DIFFRACTION-BASED SENSITIVITY ANALYSIS OF APODIZED PUPIL-MAPPING SYSTEMS

Ruslan Belikov and N. Jeremy Kasdin

Mechanical and Aerospace Engineering, Princeton University, Engineering Quad, Princeton, NJ 08544;
rbelikov@princeton.edu, jkasdin@princeton.edu

and

Robert J. Vanderbei

Operations Research and Financial Engineering, Princeton University, Princeton, NJ 08544; rvdb@princeton.edu

ABSTRACT

Pupil mapping is a promising and unconventional new method for high-contrast imaging being considered for terrestrial exoplanet searches. It employs two (or more) specially designed aspheric mirrors to create a high-contrast amplitude profile across the telescope pupil that does not appreciably attenuate amplitude. As such, it reaps significant benefits in light-collecting efficiency and inner working angle, both critical parameters for terrestrial planet detection. While much has been published on various aspects of pupil-mapping systems, the problem of sensitivity to wave front aberrations remains an open question. In this paper we present an efficient method for computing the diffraction propagation in a pupil-mapped system. This method can be used for accurate studies of aberration sensitivity in pupil mapping and other coronagraphs. We demonstrate calculations of sensitivity to Zernike aberrations for a particular pupil-mapping system, as well as a concentric-ring-shaped-pupil coronagraph.

Subject headings: planetary systems — techniques: high angular resolution

Online material: color figures

1. INTRODUCTION

The impressive discoveries of large extrasolar planets over the past decade have inspired widespread interest in finding and directly imaging Earth-like planets in the habitable zones of nearby stars. In fact, NASA has plans to launch two space telescopes to accomplish this, the *Terrestrial Planet Finder Coronagraph* (*TPF-C*) and the *Terrestrial Planet Finder Interferometer* (*TPF-I*), while the European Space Agency is planning a similar interferometer mission called *Darwin*. These missions are currently in the concept study phase. In addition, numerous ground-based searches are proceeding using both coronagraphic and interferometric approaches.

Direct imaging of Earth-like extrasolar planets in the habitable zones of Sun-like stars poses an extremely challenging problem in high-contrast imaging. Such a star will shine 10^{10} times more brightly than the planet. And, if we assume that the star-planet system is 10 pc from us, the maximum separation between the star and the planet will be roughly 0″.1.

Design concepts for TPF-C.—For *TPF-C*, for example, the current baseline design involves a traditional Lyot coronagraph consisting of a modern eighth-order occulting mask (see, e.g., Kuchner et al. 2005) attached to the back end of a Ritchey-Chretien telescope having an 8 m × 3.5 m elliptical primary mirror. Alternative innovative back-end designs still being considered include shaped pupils (see, e.g., Kasdin et al. 2003; Vanderbei et al. 2004), a visible nuller (see, e.g., Shao et al. 2004), and pupil mapping (see, e.g., Guyon [2003], where this technique is called "phase-induced amplitude apodization" or PIAA). By pupil mapping we mean a system of two lenses, or mirrors, that takes a flat input field at the entrance pupil and produces an output field that is amplitude-modified but still flat in phase (at least for on-axis sources).

The pupil-mapping concept.—The pupil-mapping concept has received considerable attention recently because of its high throughput and small effective inner working angle (IWA). These benefits could potentially permit more observations over the mission lifetime, or conversely, a smaller and cheaper overall telescope. As a result, there have been numerous studies over the past few years to examine the performance of pupil-mapping systems. In particular, Guyon (2003), Traub & Vanderbei (2003), Vanderbei & Traub (2005), and Guyon et al. (2005) derived expressions for the optical surfaces using ray optics. However, these analyses made no attempt to provide a complete diffraction through a pupil-mapping system. More recently, Vanderbei (2006) provided a detailed diffraction analysis. Unfortunately, this analysis showed that a pupil-mapping system, in its simplest and most elegant form, cannot achieve the required 10^{-10} contrast; the diffraction effects from the pupil-mapping systems themselves are so detrimental that contrast is limited to 10^{-5}. In Guyon et al. (2005) and Pluzhnik et al. (2006), a hybrid pupil-mapping system was proposed that combines the pupil-mapping mirrors with a modest apodization of oversized entrance and exit pupils. This combination does indeed achieve the needed high-contrast point-spread function (PSF). In this paper we call such systems "apodized pupil-mapping" systems.

A second problem that must be addressed is the fact that a simple two-mirror (or two-lens) pupil-mapping system introduces nonconstant angular magnification for off-axis sources (such as a planet). In fact, the off-axis magnification for light passing through a small area of the exit pupil is directly proportional to the amplitude amplification in that small area. For systems in which the exit amplitude amplification is constant, the magnification is also constant. But, for high-contrast imaging, we are interested in amplitude profiles that are far from constant. Hence, off-axis sources do not form images in a formal sense (the "images" are very distorted). Guyon (2003) proposed an elegant solution to this problem involving a reverse pupil-mapping system after the initial one to "unmap" the off-axis beam and thus remove the distortions introduced by the first system.

Sensitivity analysis.—What remains to be answered is how apodized pupil mapping behaves in the presence of optical aberrations.

It is essential that contrast be maintained during an observation, which might take hours during which the wave front will undoubtedly suffer aberration due to the small dynamic perturbations of the primary mirror. An understanding of this sensitivity is critical to the design of *TPF-C* or any other observatory. In Green et al. (2004) and Shaklan & Green (2005), a detailed sensitivity analysis is given for shaped pupils and various Lyot coronagraphs (including the eighth-order image plane mask introduced in Kuchner et al. [2005]). So far, however, no comparable study has been done for apodized pupil mapping. One obstacle to such a study is the considerable computing power required to do a full two-dimensional (2D) diffraction simulation.

Aberrations given by Zernike polynomials.—In this paper we present an efficient method for computing the effects of wave front aberrations on apodized pupil mapping. We begin with a brief review of the design of apodized pupil-mapping systems in § 2. We then present in § 3 a semianalytical approach to computing the PSF of systems such as pupil mapping and concentric rings in the presence of aberrations represented by Zernike polynomials. For such aberrations, it is possible to analytically integrate the integral over the azimuthal angle, thereby reducing the computational problem from a double integral to a single one, eliminating the need for massive computing power. In § 4 we present the sensitivity results for an example apodized pupil-mapping system and a concentric-ring-shaped-pupil coronagraph and compare the results.

2. REVIEW OF PUPIL MAPPING AND APODIZATION

In this section we review the apodized pupil-mapping approach and introduce the specific system that we study in subsequent sections. It should be noted that this apodized pupil-mapping design may not be the best possible. Rather, it is merely an example of such a system that achieves high contrast. Other examples can be found in the recent paper by Pluzhnik et al. (2006). Our aim in this paper is not to identify the best such system. Rather, our aim here is to introduce tools for carrying a full diffraction analysis of any apodized pupil-mapping system in the presence of aberrations.

2.1. *Pupil Mapping via Ray Optics*

We begin by summarizing the ray optics description of pure pupil mapping. An on-axis ray entering the first pupil at radius r from the center is to be mapped to radius $\tilde{r} = \tilde{R}(r)$ at the exit pupil (see Fig. 1). Optical elements at the two pupils ensure that the exit ray is parallel to the entering ray. The function $\tilde{R}(r)$ is assumed to be positive and increasing or, sometimes, negative and decreasing. In either case, the function has an inverse that allows us to recapture r as a function of $\tilde{r}$: $r = R(\tilde{r})$. The purpose of pupil mapping is to create nontrivial amplitude profiles. An amplitude profile function $A(\tilde{r})$ specifies the ratio between the output amplitude at $\tilde{r}$ to the input amplitude at r (in a pure pupil-mapping system the input amplitude is constant). Vanderbei & Traub (2005) showed that for any desired amplitude profile $A(\tilde{r})$ there is a pupil-mapping function $R(\tilde{r})$ that achieves it (in a ray optics sense). Specifically, the pupil mapping is given by

$$R(\tilde{r}) = \pm\sqrt{\int_0^{\tilde{r}} 2A^2(s)s\,ds}. \tag{1}$$

Furthermore, if we consider the case of a pair of lenses that are planar on their outward-facing surfaces, then the inward-facing surface profiles, $h(r)$ and $\tilde{h}(\tilde{r})$, that are required to obtain the de-

sired pupil mapping are given by the solutions to the following ordinary differential equations:

$$\frac{\partial h}{\partial r}(r) = \frac{r - \tilde{R}(r)}{|n-1|\sqrt{z^2 + [(n+1)/(n-1)]\left[r - \tilde{R}(r)\right]^2}},$$
$$h(0) = z, \tag{2}$$

$$\frac{\partial \tilde{h}}{\partial \tilde{r}}(\tilde{r}) = \frac{R(\tilde{r}) - \tilde{r}}{|n-1|\sqrt{z^2 + [(n+1)/(n-1)][R(\tilde{r}) - \tilde{r}]^2}},$$
$$\tilde{h}(0) = 0. \tag{3}$$

Here $n \neq 1$ is the refractive index, and z is the distance separating the centers ($r = 0$, $\tilde{r} = 0$) of the two lenses.

Let $S(r, \tilde{r})$ denote the distance between a point on the first lens surface r units from the center and the corresponding point on the second lens surface $\tilde{r}$ units from its center. Up to an additive constant, the optical path length of a ray that exits at radius $\tilde{r}$ after entering at radius $r = R(\tilde{r})$ is given by

$$Q_0(\tilde{r}) = S(R(\tilde{r}), \tilde{r}) + |n|\left[\tilde{h}(\tilde{r}) - h(R(\tilde{r}))\right], \tag{4}$$

where we have assumed that the ray path inside the lenses is parallel to the optical axis. Vanderbei & Traub (2005) showed that, for an on-axis source, $Q_0(\tilde{r})$ is constant and equal to $-(n-1)|z|$.[1]

2.2. *High-Contrast Amplitude Profiles*

The concept of pupil apodization for high-contrast imaging dates at least as far back as 1964 (Jacquinot & Roizen-Dossier 1964; Slepian 1965). More recently, there has been a resurging of interest in this field due to the prospects of imaging extrasolar planets (e.g., Soummer et al. 2003; Nisenson & Papaliolios 2001; Vanderbei et al. 2003).

If we assume that a collimated beam with amplitude profile $A(\tilde{r})$, such as one obtains as the output of a pupil-mapping system, is passed into an ideal imaging system with focal length f, the electric field $E(\rho)$ at the image plane is given by the Fourier transform of $A(\tilde{r})$,

$$E(\xi, \eta)$$
$$= \frac{E_0}{\lambda i f} e^{\pi i (\xi^2 + \eta^2)/\lambda f} \int_{-\infty}^{\infty} \int_{-\infty}^{\infty} e^{-2\pi i (\tilde{x}\xi + \tilde{y}\eta)/\lambda f} A\left(\sqrt{\tilde{x}^2 + \tilde{y}^2}\right) d\tilde{y}\, d\tilde{x}. \tag{5}$$

Here E_0 is the input amplitude, which, unless otherwise noted, we take to be unity. Since the optics are azimuthally symmetric, it is convenient to use polar coordinates. The amplitude profile A is a function of $\tilde{r} = (\tilde{x}^2 + \tilde{y}^2)^{1/2}$ and the image-plane electric field depends only on the image-plane radius $\rho = (\xi^2 + \eta^2)^{1/2}$:

$$E(\rho) = \frac{1}{\lambda i f} e^{\pi i (\xi^2 + \eta^2)/\lambda f} \int_0^{\infty} \int_0^{2\pi} e^{-2\pi i \cos(\theta - \phi)(\tilde{r}\rho)/\lambda f} A(\tilde{r})\tilde{r}\, d\theta\, d\tilde{r} \tag{6}$$

$$= \frac{2\pi}{\lambda i f} e^{\pi i (\xi^2 + \eta^2)/\lambda f} \int_0^{\infty} J_0\left(-2\pi \frac{\tilde{r}\rho}{\lambda f}\right) A(\tilde{r})\tilde{r}\, d\tilde{r}. \tag{7}$$

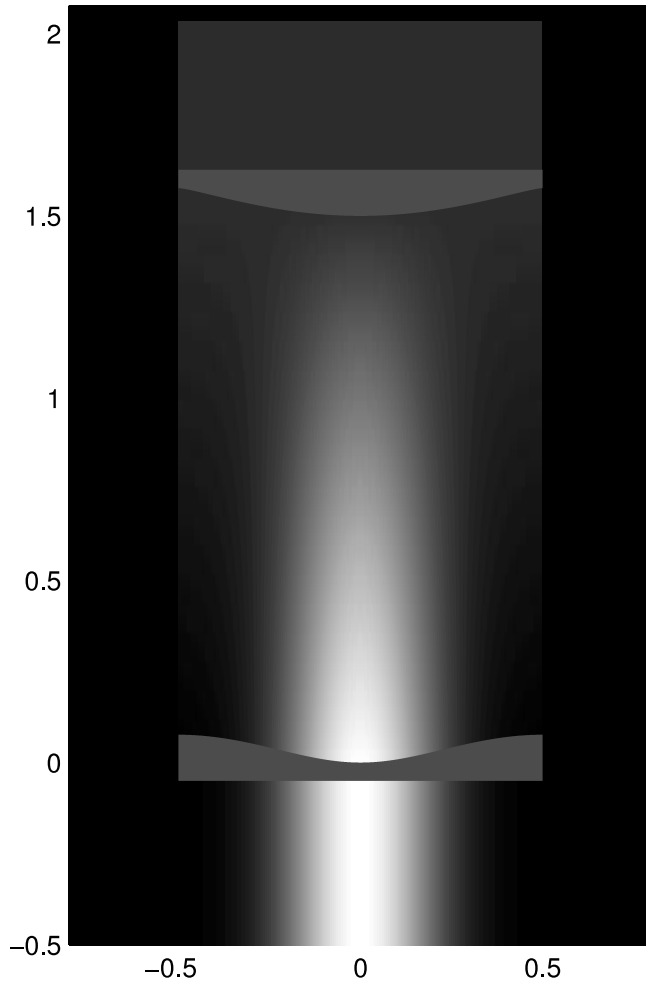[1] For a pair of mirrors, set $n = -1$. In that case, $z < 0$ as the first mirror is "below" the second.

Fig. 1.—Pupil mapping via a pair of properly figured lenses. Light travels from top to bottom.

The PSF is the square of the electric field,

$$\mathrm{PSF}(\rho) = |E(\rho)|^2. \tag{8}$$

For the purpose of terrestrial planet finding, it is important to construct an amplitude profile for which the PSF at small nonzero angles is 10 orders of magnitude reduced from its value at zero. The amplitude apodization profile used in this paper was computed using the methods in Vanderbei et al. (2003), which explains how to compute amplitude apodization functions as solutions to certain optimization problems. The high-contrast amplitude profile used in the rest of this paper is shown in Figure 2.

2.3. *Apodized Pupil-mapping Systems*

Vanderbei (2006) showed that pure pupil-mapping systems designed for a contrast of 10^{-10} actually achieve much less than this due to harmful diffraction effects that are not captured by the simple ray-tracing analysis outlined in § 2.1. For most systems of practical real-world interest (i.e., systems with apertures of a few inches and designed for visible light), contrast is limited to about 10^{-5}. Vanderbei (2006) considered certain hybrid designs that improve on this level of performance, but none of the hybrid designs presented there completely overcame this diffraction-induced contrast degradation.

In this section we describe an apodized pupil-mapping system that is somewhat more complicated than the designs presented in
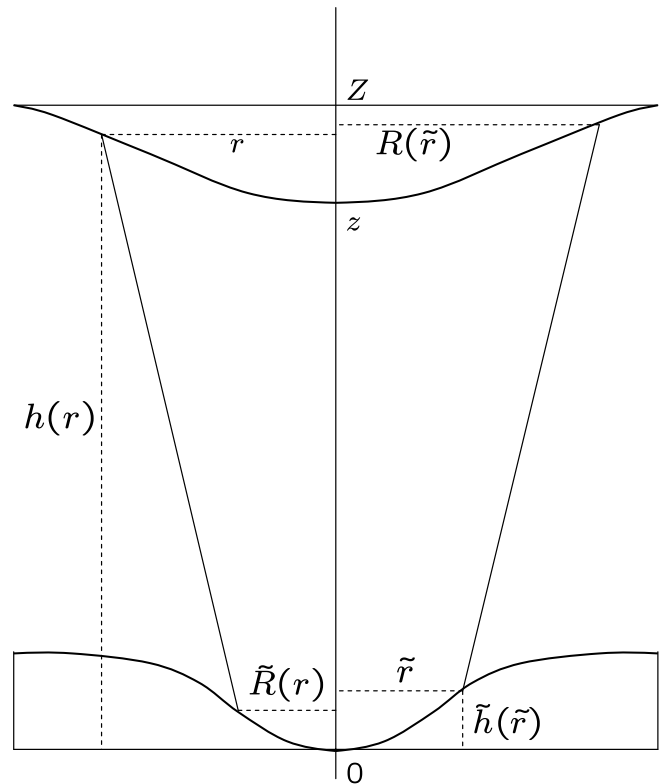
Vanderbei (2006). This is a hybrid design, because it involves several components in addition to the pure pupil-mapping system. They are

1. A preapodizer A_0 to soften the edge of the first lens/mirror so as to minimize diffraction effects caused by hard edges.
2. A postapodizer to smooth out low spatial frequency ripples produced by diffraction effects induced by the pupil-mapping system itself.
3. A back-end phase shifter to smooth out low spatial frequency ripples in phase.

Note that the back-end phase shifter can be built into the second lens/mirror, in which case our hybrid system consists of two classical apodizers and a pure pupil-mapping system.

A similar setup is presented in Pluzhnik et al. (2006), in which the authors describe how and why apodizers mitigate diffraction in pupil mapping and suggest how to optimize a hybrid design. We have not yet attempted such optimizations but rather present an example here that we have found to achieve 10^{10} contrast. Our apodizers and mirror profiles are different from the design in Pluzhnik et al. (2006), and we do not oversize our mirrors. Our preapodizer has the following form (the same as the postapodizer described by eqs. [3] and [4] in Pluzhnik et al. [2006]):

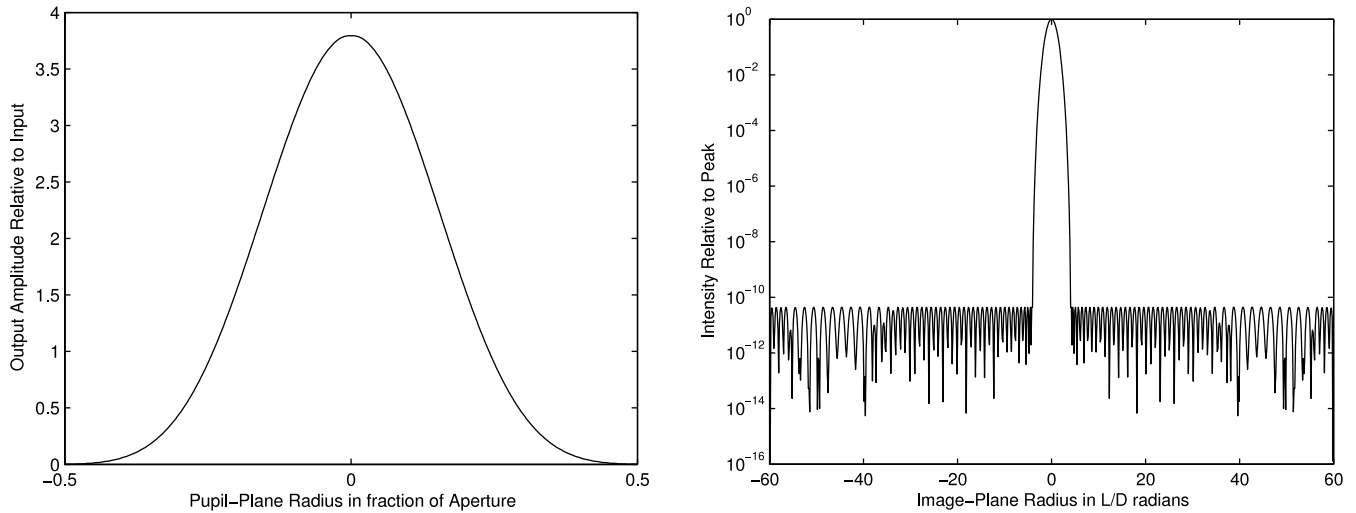$$A_0(r) = \frac{A(r)(1 + \beta)}{A(r) + \beta A_{\max}},$$

Fig. 2.—*Left:* Amplitude profile providing contrast of 10^{-10} at tight IWAs. *Right:* Corresponding on-axis PSF.

where $A_{\max}$ denotes the maximum value of $A(r)$ and β is a scalar parameter, which we take to be 0.1. It is easy to see that

1. $A(r)/A_{\max} \le A_0(r) \le 1$ for all r.
2. $A_0(r)$ approaches 1 as $A(r)$ approaches $A_{\max}$.
3. $A_0(r)$ approaches 0 as $A(r)$ approaches 0.

Incorporating a postapodizer introduces a degree of freedom that is lacking in a pure pupil-mapping system. Namely, it is possible to design the pupil-mapping system based on an arbitrary amplitude profile and then convert this profile to a high-contrast profile via an appropriate choice of back-end apodizer. We have found that a simple Gaussian amplitude profile that approximately matches a high-contrast profile works very well. Specifically, we use

$$A_{\text{pupmap}}(\tilde{r}) = 3.35 e^{-22(\tilde{r}/D)^2},$$

where D denotes the diameter of the input beam and the lenses/mirrors.

The back-end apodization is computed by taking the actual output amplitude profile as computed by a careful diffraction analysis, smoothing it by convolution with a Gaussian distribution, and then apodizing according to the ratio of the desired high-contrast amplitude profile $A(\tilde{r})$ divided by the smoothed output profile. Of course, since a true apodization can never intensify a beam, this ratio must be further scaled down so that it is nowhere greater than unity. The Gaussian convolution kernel we used has mean zero and standard deviation $D/(100,000)^{1/2}$.

The back-end phase modification is computed by a similar smoothing operation applied to the output phase profile. Of course, the smoothed output phase profile (measured in radians) must be converted to a surface profile (having units of length). This conversion requires us to assume a certain specific wavelength. As a consequence, the resulting design is correct only at one wavelength. The ability of the system to achieve high contrast degrades as one moves away from the design wavelength.

2.4. *Star Occulter and Reversed System*

It is important to note that the PSFs in Figure 2 correspond to a bright on-axis source (i.e., a star). Off-axis sources, such as faint planets, undergo two effects in a pupil-mapping system that differ from the response of a conventional imaging system: an effective magnification and a distortion. These are explained in detail

in Vanderbei & Traub (2005) and Traub & Vanderbei (2003). The magnification, in particular, is due to an overall narrowing of the exit pupil as compared to the entrance pupil. It is this magnification that provides pupil-mapped systems their smaller effective IWA. The techniques in § 3 allow us to compute the exact off-axis diffraction pattern of an apodized pupil-mapped coronagraph and thus to see these effects.

While the effective magnification of a pupil-mapping system results in an IWA advantage of about a factor of 2, it does not produce high-quality diffraction-limited images of off-axis sources because of the distortion inherent in the system. As mentioned earlier, Guyon (2003) proposed the following solution to this problem. He suggested using this system merely as a mechanism for concentrating (on-axis) starlight in an image plane. He then proposed that an occulter be placed in the image plane to remove the starlight. All other light, such as the distorted off-axis planet light, would be allowed to pass through the image plane. On the back side would be a second, identical pupil-mapping system (with the apodizers removed) that would "unmap" the off-axis beam and thus remove the distortions introduced by the first system (except for some beam walk; see Vanderbei & Traub 2005). A schematic of the full system (without the occulter) is shown in Figure 3. Our apodization is designed to concentrate most of the light into an IWA of $4\lambda/D$ (where $D = 0.025$ m is the diameter of the input beam) and that is the radius of the occulter we chose to use in our design. Note that we have spaced the lenses one focal length from the flat sides of the two lenses. As noted in Vanderbei & Traub (2005), such a spacing guarantees that these two flat surfaces form a conjugate pair of pupils.

3. DIFFRACTION ANALYSIS

In Vanderbei (2006) it was shown that a simple Fresnel analysis is inadequate for validating the high-contrast imaging capabilities we seek. Hence, a more accurate approximation was presented. In this section we give a similar but slightly different approximation that is just as effective for studying pupil mapping but is better suited to the full system we wish to analyze.

3.1. *Propagation of General Wave Fronts*

The goal of this section is to derive an integral that describes how to propagate a scalar electric field from one plane perpendicular to the direction of propagation to another parallel plane positioned downstream of the first. We assume that the electric
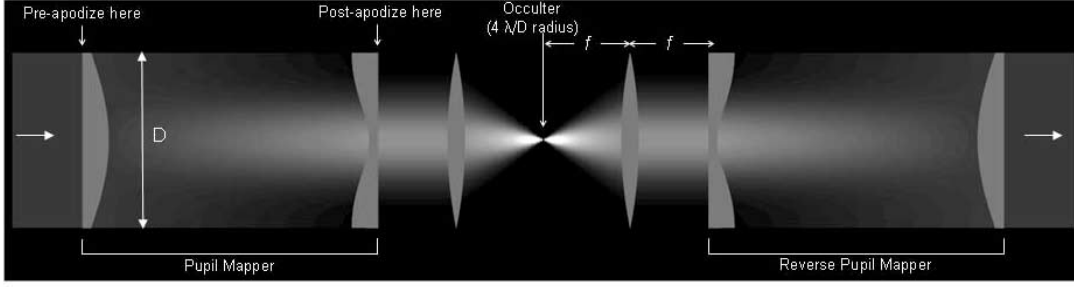
Fig. 3.—Full pupil-mapping system, including a pair of lenses with a pre- and postapodizer to shape the amplitude into a prolate-spheroidal-like amplitude profile, a focusing lens that concentrates the on-axis starlight into a small central lobe where an occulter blocks this light, followed by a recollimating lens, and finally, a reverse pupil-mapping system that reforms the pupil with the starlight removed but any planet light (if present) intact. This final pupil is then fed a final focusing element (not shown) to form an image of off-axis sources.

field passes through a lens at the first plane then propagates through free space until reaching a second lens at the second plane through which it passes. In order to cover the apodized pupil-mapping case discussed in § 2.3, we allow both the entrance and exit fields to be apodized.

Suppose that the input field at the first plane is $E_{in}(x, y)$. Then the electric field at a particular point on the second plane can be well approximated by superimposing the phase-shifted waves from each point across the entrance pupil (this is the well-known Huygens-Fresnel principle; see, e.g., § 8.2 in Born & Wolf 1999). If we assume that the two lenses are given by radial "height" functions $h(r)$ and $\tilde{h}(\tilde{r})$, then we can write the exit field as

$$E_{out}(\tilde{x}, \tilde{y}) = A_{out}(\tilde{r}) \int_{-\infty}^{\infty} \int_{-\infty}^{\infty} \frac{1}{\lambda i Q(\tilde{x}, \tilde{y}, x, y)}$$
$$\times e^{2\pi i Q(\tilde{x}, \tilde{y}, x, y)/\lambda} A_{in}(r) E_{in}(x, y) \, dy \, dx, \quad (9)$$

where

$$Q(\tilde{x}, \tilde{y}, x, y) = \sqrt{(x - \tilde{x})^2 + (y - \tilde{y})^2 + [h(r) - \tilde{h}(\tilde{r})]^2}$$
$$+ |n| [Z - h(r) + \tilde{h}(\tilde{r})] \quad (10)$$

is the optical path length, Z is the distance between the planar lens surfaces, $A_{in}(r)$ denotes the input amplitude apodization at radius r, and $A_{out}(\tilde{r})$ denotes the output amplitude apodization at radius $\tilde{r}$, and where, of course, we have used r and $\tilde{r}$ as shorthand for the radii in the entrance and exit planes, respectively.

As before, it is convenient to work in polar coordinates:

$$E_{out}(\tilde{r}, \tilde{\theta}) = A_{out}(\tilde{r}) \int_0^{\infty} \int_0^{2\pi} \frac{1}{\lambda i Q(\tilde{r}, r, \theta - \tilde{\theta})}$$
$$\times e^{2\pi i Q(\tilde{r}, r, \theta - \tilde{\theta})/\lambda} A_{in}(r) E_{in}(r, \theta) r \, d\theta \, dr, \quad (11)$$

where

$$Q(\tilde{r}, r, \theta) = \sqrt{r^2 - 2r\tilde{r} \cos \theta + \tilde{r}^2 + [h(r) - \tilde{h}(\tilde{r})]^2}$$
$$+ |n| [Z - h(r) + \tilde{h}(\tilde{r})]. \quad (12)$$

For numerical tractability, it is essential to make approximations so that the integral over θ can be carried out analytically, thereby reducing the double integral to a single one. To this

end, we need to make an appropriate approximation to the square-root term:

$$S = \sqrt{r^2 - 2r\tilde{r} \cos \theta + \tilde{r}^2 + [h(r) - \tilde{h}(\tilde{r})]^2}. \quad (13)$$

A simple crude approximation is adequate for the $1/Q(\tilde{r}, r, \theta - \tilde{\theta})$ amplitude-reduction factor in equation (11). We approximate this factor by the constant $1/Z$.

The $Q(\tilde{r}, r, \theta - \tilde{\theta})$ appearing in the exponential must, on the other hand, be treated with care. The classical Fresnel approximation is to replace S by the first two terms in a Taylor series expansion of the square-root function about $[h(r) - \tilde{h}(\tilde{r})]^2$. As we already mentioned, this approximation is too crude. It is critically important that the integrand be exactly correct when the pair $(r, \tilde{r})$ corresponds to rays of ray optics. Here is a method that does this. First, we add and subtract $S(\tilde{r}, r, 0)$ from $Q(\tilde{r}, r, \theta)$ in equation (12) to get

$$Q(\tilde{r}, r, \theta - \tilde{\theta}) = S(\tilde{r}, r, \theta - \tilde{\theta}) - S(\tilde{r}, r, 0)$$
$$+ S(\tilde{r}, r, 0) + |n| [\tilde{h}(\tilde{r}) - h(r)]$$
$$= \frac{S(\tilde{r}, r, \theta - \tilde{\theta})^2 - S(\tilde{r}, r, 0)^2}{S(\tilde{r}, r, \theta - \tilde{\theta}) + S(\tilde{r}, r, 0)}$$
$$+ S(\tilde{r}, r, 0) + |n| [\tilde{h}(\tilde{r}) - h(r)]$$
$$= \frac{r\tilde{r} - r\tilde{r} \cos (\theta - \tilde{\theta})}{[S(\tilde{r}, r, \theta - \tilde{\theta}) + S(\tilde{r}, r, 0)]/2}$$
$$+ S(\tilde{r}, r, 0) + |n| [\tilde{h}(\tilde{r}) - h(r)]. \quad (14)$$

So far, these calculations are exact. The only approximation we now make is to replace $S(\tilde{r}, r, \theta - \tilde{\theta})$ in the denominator of equation (14) with $S(\tilde{r}, r, 0)$ so that the denominator becomes just $S(\tilde{r}, r, 0)$. Putting this all together, we get a new approximation, which we refer to as the "S-Huygens" approximation:

$$E_{out}(\tilde{r}, \tilde{\theta}) \approx \frac{1}{\lambda i Z} \int_0^{\infty} K(r, \tilde{r})$$
$$\times \int_0^{2\pi} e^{2\pi i [-\tilde{r} r \cos(\theta - \tilde{\theta})/S(\tilde{r}, r, 0)]/\lambda} E_{in}(r, \theta) \, d\theta \, r \, dr, \quad (15)$$

where

$$K(r, \tilde{r}) = A_{out}(\tilde{r}) e^{2\pi i \{ r\tilde{r}/S(\tilde{r}, r, 0) + S(\tilde{r}, r, 0) + |n| [\tilde{h}(\tilde{r}) - h(r)] \}/\lambda} A_{in}(r)$$
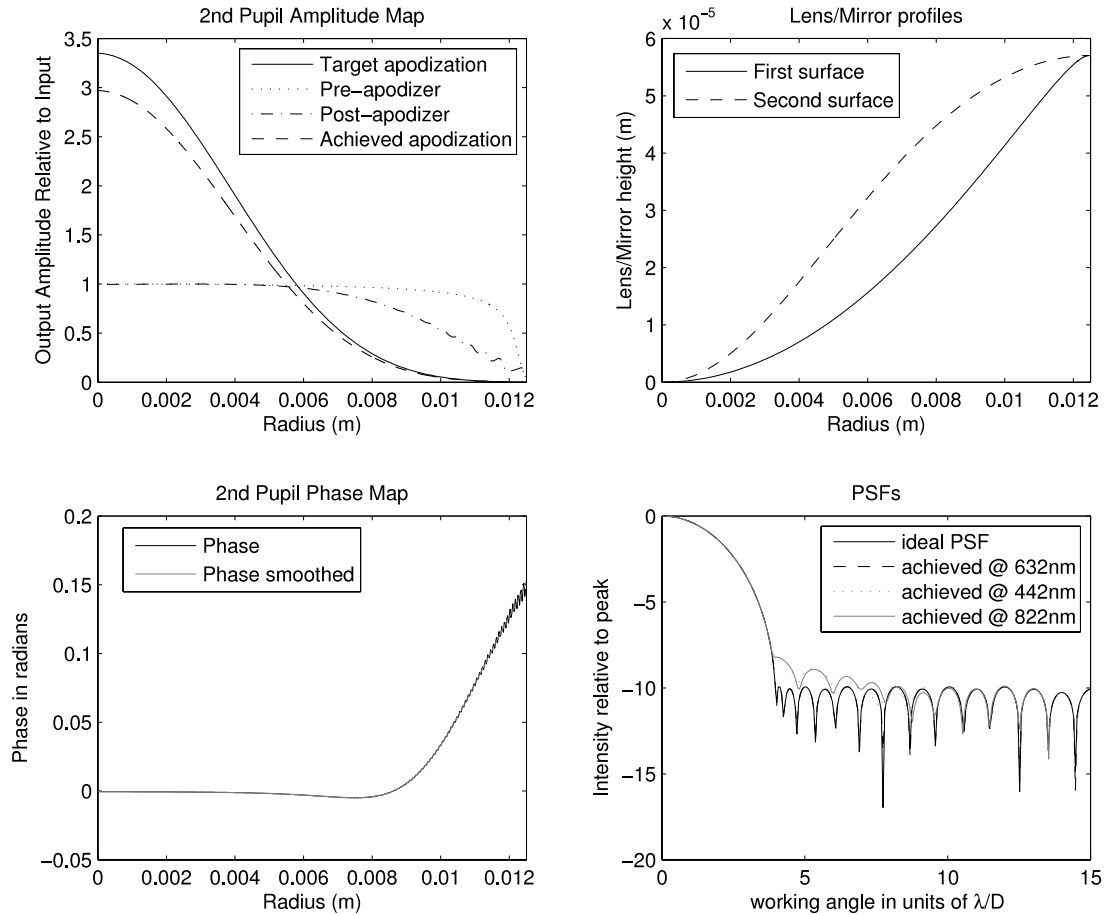$$(16)$$

Fig. 4.—Analysis of an apodized pupil-mapping system using the S-Huygens approximation with $z = 15D$ and $n = 1.5$. *Top left:* Target high-contrast amplitude profile (*solid line*) and the amplitude profile computed using the S-Huygens approximation through the apodized pupil-mapping system (*dashed line*). The other two lines depict the pre- and postapodizers. *Top right:* Lens profiles, solid line for the first lens and dashed for the second. The lens profiles h and $\tilde{h}$ were computed using a 5000 point discretization. *Bottom left:* Phase map computed using the S-Huygens propagation with a 5000 point discretization. This line exhibits high-frequency oscillations that are smoothed before computing the postapodizer to help with chromaticity. *Bottom right:* PSF computed at three different wavelengths; the design value, 30% above that value, and 30% below it. [*See the electronic edition of the Journal for a color version of this figure.*]

[note that we have dropped an $\exp{(2\pi i n Z/\lambda)}$ factor, since this factor is just a constant unit complex number that would disappear anyway at the end when we compute intensities].

The only reason for making approximations to the Huygens-Fresnel integral equation (9) is to simplify the dependence on θ so that the integral over this variable can be carried out analytically. For example, if we now assume that the input field $E_{in}(r, \theta)$ does not depend on θ, then the inner integral can be evaluated explicitly, and we get

$$E_{out}(\tilde{r}, \tilde{\theta}) \approx \frac{2\pi}{\lambda i Z} \int_0^\infty K(r, \tilde{r}) J_0\left(\frac{2\pi\tilde{r}r}{\lambda S(\tilde{r}, r, 0)}\right) E_{in}(r) r \, dr. \quad (17)$$

Removing the dependency on θ greatly simplifies computations, because we only need to compute a one-dimensional (1D) integral instead of 2D. In § 3.2 we show how to achieve similar reductions in cases in which the dependence of E_{in} on θ takes a simple form.

Figure 4 shows plots characterizing the performance of an apodized pupil-mapping system analyzed using the techniques described in this section. The specifications for this system are as follows. The designed for wavelength is 632.8 nm. The optical elements are assumed to be mirrors separated by 0.375 m. The

system is an on-axis system, and we therefore make the nonphysical assumption that the mirrors do not obstruct the beam. That is, the mirrors are invisible except when they are needed. The mirrors take as input a 0.025 m on-axis beam and produce a 0.025 m pupil-remapped exit beam. They are both 0.025 m in diameter, and both the pre and postapodizer taper down to the value 0 along the circumference of the mirrors as shown in Figure 4, in order to mitigate the diffraction effects due to sharp edges. After the second mirror, the exit beam is brought to a focus. The focal length is 2.5 m. Figure 4 (*bottom right*) shows the ideal PSF (*black*) together with the achieved PSF at three wavelengths: at 70%, 100%, and 130% of the design wavelength. At the design wavelength, the achieved PSF matches the ideal PSF almost exactly. Note that there is minor degradation at the other two wavelengths mostly at low spatial frequencies.

We end this section by pointing out that the S-Huygens approximation given by equation (15) is the basis for all subsequent analysis in this paper. It can be used to compute the propagation between every pair of consecutive components in apodized pupil-mapping and concentric-ring systems. It should be noted that the approximation does not reduce to the standard Fresnel or Fourier approximations even when considering such simple scenarios as free-space propagation of a plane wave or propagation from a pupil plane to an image plane. Even for these elementary situations, the

S-Huygens approximation is more accurate than the usual text-book approximations.

3.2. *Propagation of Azimuthal Harmonics*

In this section we assume that $E(r, \theta) = E(r)e^{ik\theta}$ for some integer k. We refer to such a field as a "kth-order azimuthal harmonic." We show that a kth-order azimuthal harmonic will remain a kth-order azimuthal harmonic after propagating from the input plane to the output plane described in § 3.1. Only the radial component $E(r)$ changes, which enables the reduction of the computation from 2D to 1D. Arbitrary fields can also be propagated, by decomposing them into azimuthal harmonics and propagating each azimuthal harmonic separately. Computation is thus greatly simplified even for arbitrary fields, especially for the case of fields that can be described by only a few azimuthal harmonics to a high precision, such as Zernike aberrations, which we consider in § 3.3. This improvement in computational efficiency is important, because a full 2D diffraction simulation of an apodized pupil-mapping system with a precision greater than 10^{10} typically overwhelms the memory of a mainstream computer. By reducing the computation from 2D to 1D, however, the entire apodized pupil-mapping system can be simulated with negligible memory requirements and takes only minutes.

Theorem 1. Suppose that the input field in an optical system described by equation (15) is a kth-order azimuthal harmonic $E_{in}(r, \theta) = E_i(r)e^{ik\theta}$ for some integer k. Then the output field is also a kth-order azimuthal harmonic $E_{out}(\tilde{r}, \tilde{\theta}) = E_o(\tilde{r})e^{ik\tilde{\theta}}$ with radial part given by

$$E_o(\tilde{r}) = \frac{2\pi}{i^{k+1}\lambda Z} \int_0^\infty K(r, \tilde{r}) E_i(r) J_k\left(\frac{2\pi r\tilde{r}}{\lambda S(\tilde{r}, r, 0)}\right) r\, dr.$$

Proof. We start by substituting the azimuthal harmonic form of E_{in} into equation (15) and regrouping factors to get

$$E_{out}(\tilde{r}, \tilde{\theta}) = \frac{1}{i\lambda Z} \int_0^\infty K(r, \tilde{r})$$
$$\times \int_0^{2\pi} e^{2\pi i\left[-\tilde{r}r\cos(\theta-\tilde{\theta})/S(\tilde{r}, r, 0)\right]/\lambda} E_i(r)e^{ik\theta}\, d\theta\, r\, dr$$
$$= \left\{ \frac{1}{i\lambda Z} \int_0^\infty K(r, \tilde{r}) E_i(r) \right.$$
$$\left. \times \int_0^{2\pi} e^{2\pi i\left[-\tilde{r}r\cos(\theta-\tilde{\theta})/S(\tilde{r}, r, 0)\right]/\lambda} e^{ik(\theta-\tilde{\theta})}\, d\theta\, r\, dr \right\} e^{ik\tilde{\theta}}.$$
$$(18)$$

The result then follows from an explicit integration over the θ variable:

$$E_{out}(\tilde{r}, \tilde{\theta}) = \left[\frac{2\pi}{i^{k+1}\lambda Z} \int_0^\infty K(r, \tilde{r}) E_i(r) \right.$$
$$\left. \times J_k\left(\frac{2\pi r\tilde{r}}{\lambda S(\tilde{r}, r, 0)}\right) r\, dr \right] e^{ik\tilde{\theta}}.$$

3.3. *Decomposition of Zernike Aberrations into Azimuthal Harmonics*

The theorem shows that the full 2D propagation of azimuthal harmonics can be computed efficiently by evaluating a 1D integral. However, suppose that the input field is not an azimuthal harmonic but something more familiar, such as a (l, m) Zernike aberration,

$$E_{in}(r, \theta) = e^{i\epsilon Z_l^m(2r/D)\cos(m\theta)},$$
$$(19)$$

where ϵ is a small number ($\epsilon/2\pi$ and ϵ/π are the peak-to-valley phase variations across the aperture of diameter D for $m = 0$ and $m \neq 0$, respectively).

Recall that the definition of the kth-order Bessel function is

$$J_k(x) = \frac{1}{2\pi i^k} \int_0^{2\pi} e^{ix\cos\theta} e^{ik\theta}\, d\theta.$$
$$(20)$$

From this definition we see that $i^k J_k(x)$ are simply the Fourier coefficients of $e^{ix\cos(\theta)}$. Hence, the Fourier series for the complex exponential is given simply by the so-called Jacobi-Anger expansion

$$e^{ix\cos\theta} = \sum_{k=-\infty}^\infty i^k J_k(x)e^{ik\theta}.$$
$$(21)$$

The Zernike aberration can be decomposed into azimuthal harmonics using the Jacobi-Anger expansion:

$$e^{i\epsilon Z_l^m(2r/D)\cos(m\theta)} = \sum_{k=-\infty}^\infty i^k J_k\left(\epsilon Z_l^m(2r/D)\right)e^{ikm\theta}$$
$$(22)$$

$$= J_0\left(\epsilon Z_l^m(2r/D)\right) + \sum_{k=1}^\infty i^k J_k\left(\epsilon Z_l^m(2r/D)\right)e^{ikm\theta}.$$
$$(23)$$

Note that

$$|J_k(x)| \approx \frac{1}{k!}\left(\frac{x}{2}\right)^k$$

for $0 \leq x \ll 1$. Hence, if we assume that $\epsilon \sim 10^{-3}$, then the kth term is on the order of 10^{-3k}. The field amplitude in the high-contrast region of the PSF is dominated by the $k = 1$ term and is on the order of 10^{-3}. If we drop terms of $k = 3$ and above, we are introducing an error on the order of 10^{-9} in amplitude. The error in intensity is dominated by a cross product of the $k = 3$ and the $k = 1$ term, or 10^{-12} across the dark region. So, in this case, Zernike aberrations can be more than adequately modeled using just three azimuthal harmonic terms. For $\epsilon \sim 10^{-2}$, the number of terms goes up to five for an error tolerance of 10^{-12}. In practice, even this small number of terms was actually found to be overly conservative.

In order to compute the full 2D response for a given Zernike aberration, we simply decompose it into a few azimuthal harmonics, propagate them separately, and sum the results at the end. This method could also be applied to any arbitrary field.

4. SIMULATIONS

The entire four-mirror apodized pupil-mapping system can be modeled as the following sequence of seven steps:

1. Propagate an input wave front from the front (flat) surface of the first pupil-mapping lens to the back (flat) surface of the second pupil-mapping lens as described in § 3.

2. Propagate forward a distance f.

3. Propagate through a positive lens with focal length f to a focal plane f units downstream.
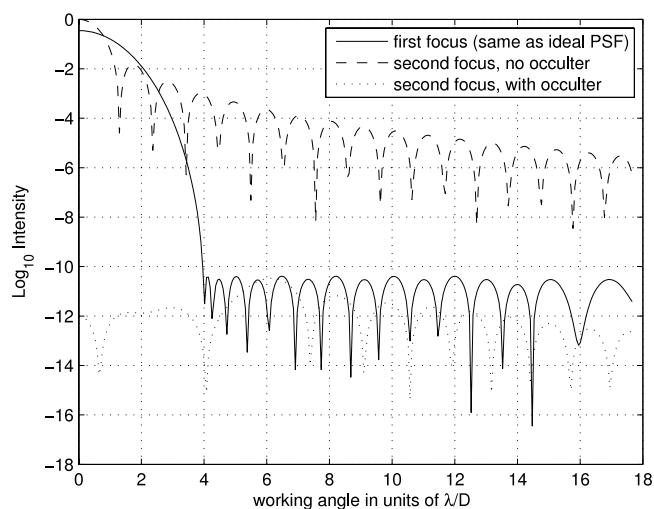
Fig. 5.—On-axis PSF at first focus (before occulter) and at second focus for cases with and without occulter. Without the occulter, the second-focus PSF almost perfectly matches the usual Airy pattern. However, with the occulter, the second-focus on-axis PSF is suppressed by 10 orders of magnitude. [*See the electronic edition of the Journal for a color version of this figure.*]

Fig. 7.—Cross-sectional plots from the second-row plots in Fig. 6. Note that for angles of $3\lambda/D$ and above, the restored PSF looks very much like an Airy pattern with very little energy attenuation. However, as the angle decreases, the pattern begins to distort and the throughput begins to diminish. [*See the electronic edition of the Journal for a color version of this figure.*]

4. Multiply by the star occulter.

5. Propagate through free-space a distance f then through a positive lens to recollimate the beam.

6. Propagate forward a distance f.

7. Propagate backward through a pupil-mapping system having the same parameters as the first one.

A similar analysis can be carried out for a concentric-ring-shaped-pupil system, or even a pure apodization system, as follows:

1. Choose A_{in} to represent either the concentric-ring binary mask or some other azimuthally symmetric apodization.

2. Choose h as appropriate for a focusing lens, and let $\tilde{h} \equiv 0$.

3. Propagate through this system a distance f to the image plane.

4. Multiply by the star occulter.

The theorem can be applied to every propagation step, so that an azimuthal harmonic will remain an azimuthal harmonic throughout the entire system. Hence, our computation strategy is to decompose the input field into azimuthal harmonics, propagate each one separately through the entire system by repeated applications of the theorem, and sum them at the very end.

Figure 5 shows a cross section plot of the PSF as it appears at first focus and second focus in our apodized pupil-mapping system (the first-focus plot is indistinguishable from the case of ideal
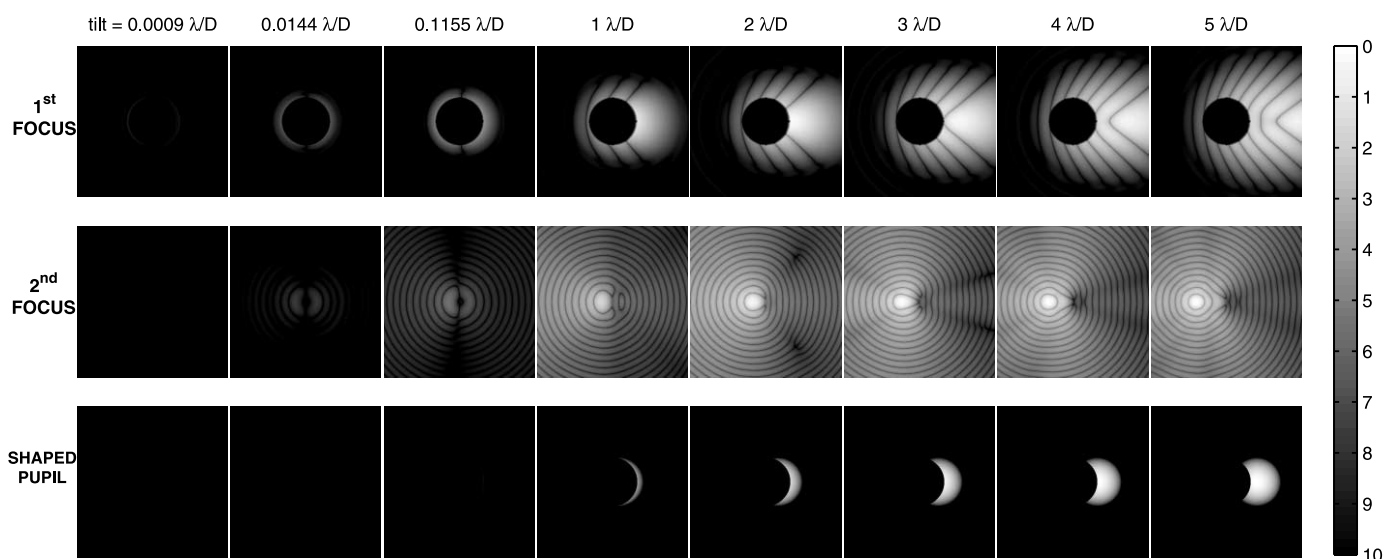

Fig. 6.—Simulated responses due to off-axis sources in apodized pupil mapping and concentric rings. *First row:* Pupil mapping, first focus, after the occulter. *Second row:* Pupil mapping, second focus (note the expected mirror flip). *Third row:* Concentric-ring coronagraph. The columns in this figure represent different off-axis source angles, labeled on the top. All the images represent the same physical area on a CCD, and the optical axis is in the exact center of each image. The dark circles in the centers of the images on the top and bottom rows are the occulters, with radius of $4f\,\lambda/D$. The intensity scale is logarithmic, spanning 10 orders of magnitude, as shown on the right. The normalization is to the peak value of the Airy PSF in the case of no coronagraph. [*See the electronic edition of the Journal for a color version of this figure.*]
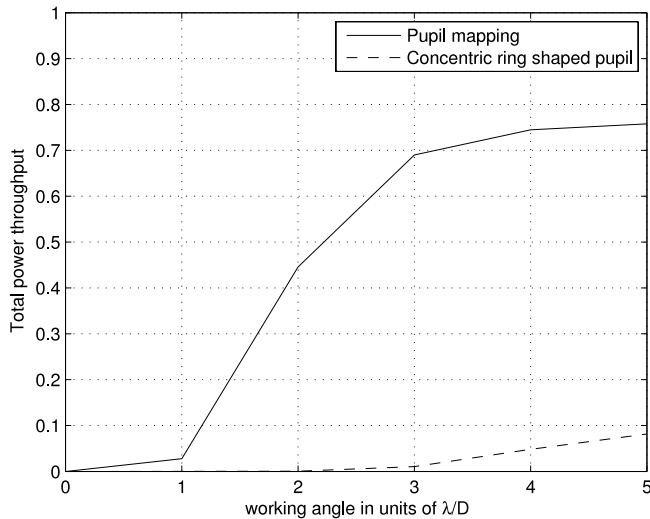
FIG. 8.—Off-axis source attenuation as a function of angle (total throughput). Note that the 50% point occurs at about $2\lambda/D$. [*See the electronic edition of the Journal for a color version of this figure.*]

apodization or concentric-ring-shaped-pupils). There are two plots for second focus: one with the occulter in place and one without it. Note that without the occulter, the PSF matches almost perfectly the usual Airy pattern. With the occulter, the on-axis light is suppressed by 10 orders of magnitude.

The most basic aberration to simulate is a tilt [i.e., the (1, 1) Zernike], which is equivalent to an off-axis source at angle (ϵ/π) (λ/D) rad. In Figure 6 we show images at the first and second focal planes of our apodized pupil-mapping system, as well as for the concentric-ring-shaped-pupil coronagraph for various tilt angles. The first three columns are for small tilt angles corresponding to the small pointing error of the telescope. The hybrid pupil-mapping system we used has more degradation than the concentric-ring pupil mask. Tilts $1\lambda/D$ and larger, shown in the following five columns, represent off-axis sources such as a planet. As discussed earlier, off-axis sources do not form good images at the first focus of pupil mapping, and this is clearly evident in the top row of Figure 6. At the second focus, however, the off-axis PSF is mostly restored, and the images begin to look like standard Airy patterns as the angle increases from about $2\lambda/D$ outward. These "Airy patterns" both are sharper and have larger peak brightness than their counterparts at first focus, just as in Figure 5. (In practice, only the main lobe of this Airy pattern is likely to be seen, because planets are so dim.) Corresponding cross-sectional plots are shown in Figure 7.

In the case of the shaped pupil, the planet PSF is also not distorted, but it is significantly less sharp and less bright than that
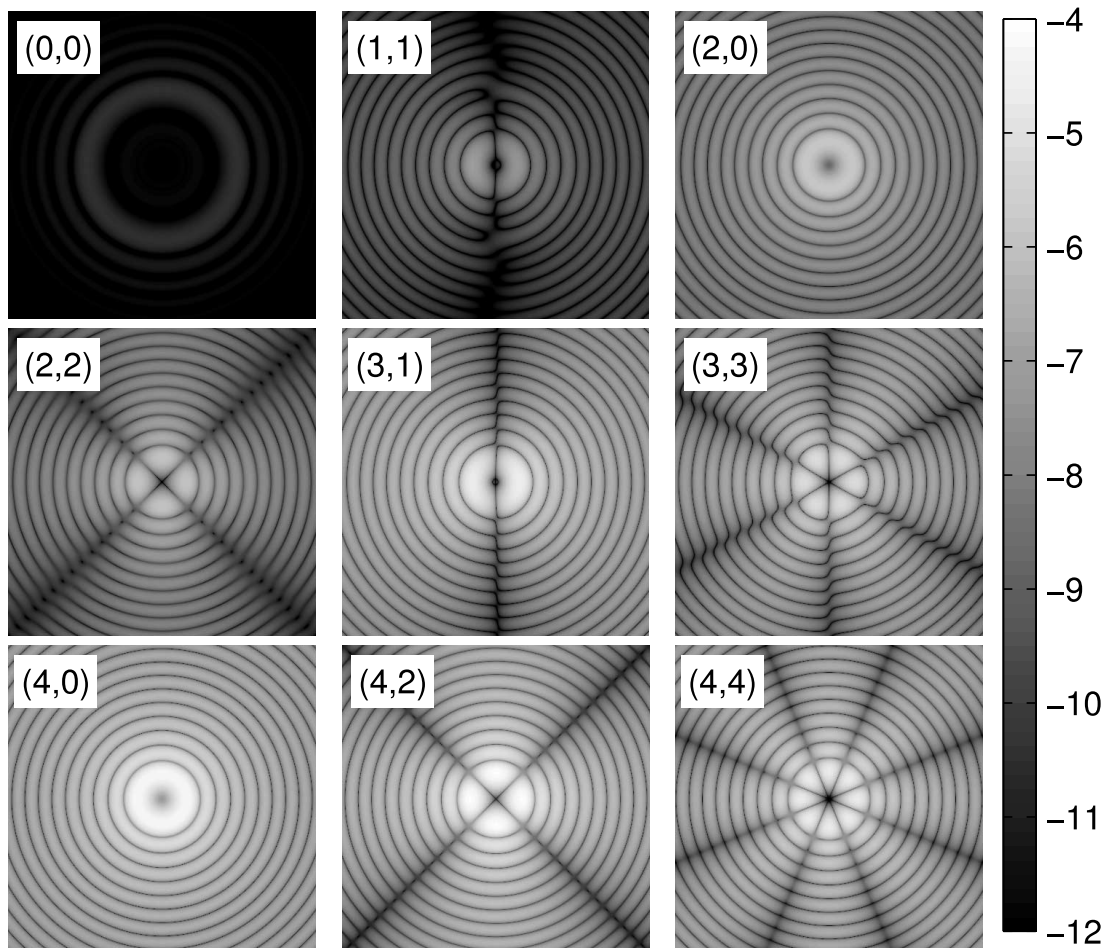

FIG. 9.—Apodized pupil-mapping sensitivities to the first nine Zernike aberrations. In each case, the rms error is 1/100 of a wave. The plots correspond to piston (0, 0), tilt (1, 1), defocus (2, 0), astigmatism (2, 2), coma (3, 1), trefoil (3, 3), spherical aberration (4, 0), astigmatism second order (4, 2), tetrafoil (4, 4). [*See the electronic edition of the Journal for a color version of this figure.*]
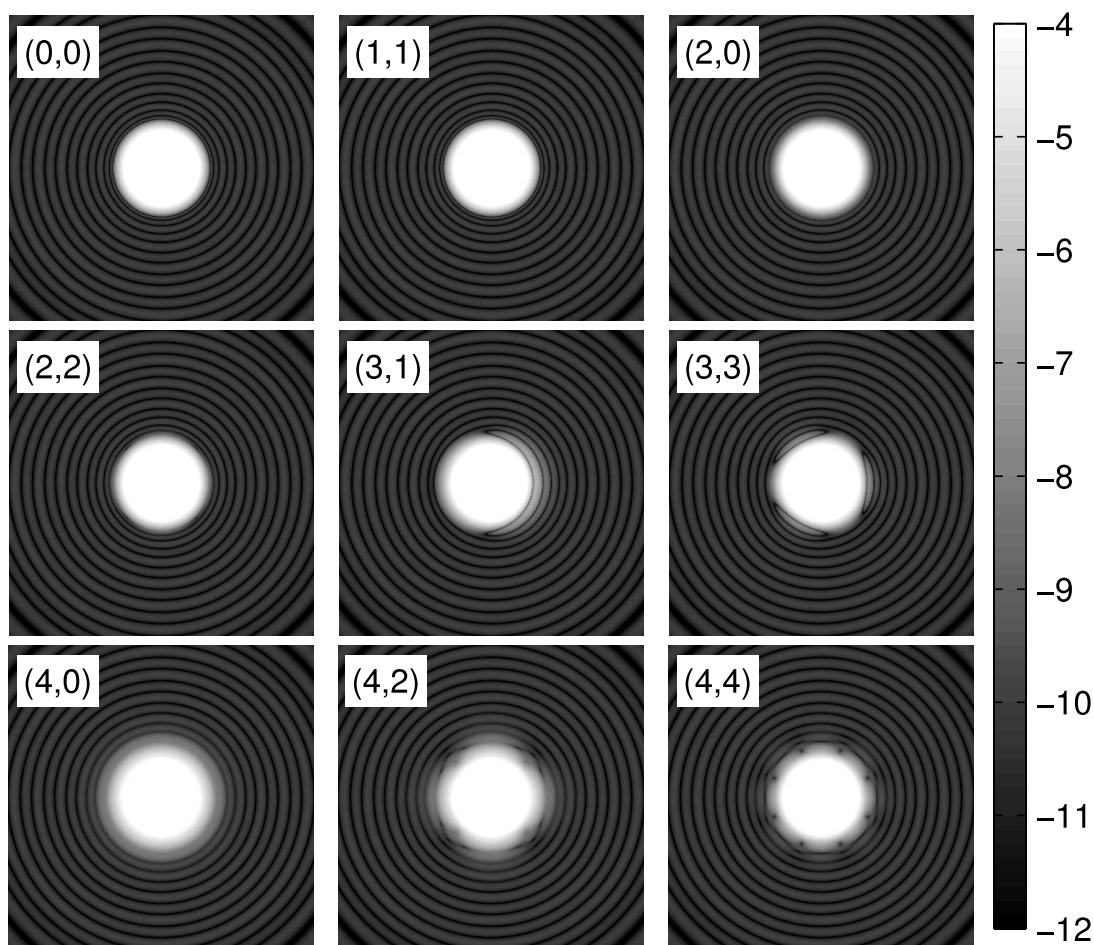
Fɪɢ. 10.—Concentric-ring mask sensitivities to the first nine Zernike aberrations. [*See the electronic edition of the Journal for a color version of this figure.*]

of the pupil mapping at second focus, as shown in the bottom row of Figure 6. It is also mostly covered by the occulter for tilts smaller than $4\lambda/D$. This clearly shows the throughput and IWA advantages of pupil mapping.

Figure 8 shows how the off-axis source is attenuated as a function of the angle from the optical axis, for the case of our apodized pupil-mapping system (at second focus) and the concentric-ring coronagraph. For the case of apodized pupil mapping, the 50% point occurs at about $2.2\lambda/D$.

Figures 9 and 10 show the distortions/leakage from an on-axis source in the presence of various Zernike aberrations, for the apodized pupil-mapping and the concentric-ring-shaped-pupil systems, respectively. The Zernike aberrations are assumed to be 1/100 wave rms.

Figure 11 shows the corresponding cross section sensitivity plots for both the apodized pupil-mapping system and the concentric-ring-shaped-pupil system. From this plot it is easy to see both the tighter IWA of apodized pupil-mapping systems and their increased sensitivity to wave front errors. Finally, Figure 12 demonstrates contrast degradation measured at three angles, $2\lambda/D$, $4\lambda/D$, and $8\lambda/D$, as a function of severity of the Zernike wave front error. The rms error is expressed in waves.

5. CONCLUSIONS

We have presented an efficient method for calculating the diffraction of aberrations through optical systems such as apodized pupil mapping and concentric-ring-shaped-pupil coronagraphs. We presented an example for both systems and computed their off-axis responses and aberration sensitivities. Figures 11 and 12 show that our particular apodized pupil-mapping system is more sensitive to low-order aberrations than the concentric-ring masks. That is, contrast and IWA degrade more rapidly with an increasing rms level of the aberrations. Thus, for a particular telescope, our pupil-mapping system will achieve better throughput and IWA but suffer greater aberration sensitivity.

We note that there is a spectrum of apodized pupil-mapping systems, out of which we selected but one example. The two extremes, pure apodization and pure pupil mapping, both have serious drawbacks. On the one end, pure apodization loses almost an order of magnitude in throughput and suffers from an unpleasantly large IWA. At the other extreme, pure pupil mapping fails to achieve the required high contrast due to diffraction effects. There are several points along this spectrum that are superior to the end points. We have focused on just one such point and leave it to future work to determine if this is the best design point. For example, clearly one can improve the aberration sensitivity by relaxing the IWA and throughput requirements. Such analysis is beyond the scope of this paper, but we have provided here the tools to analyze the sensitivity of these kinds of designs.
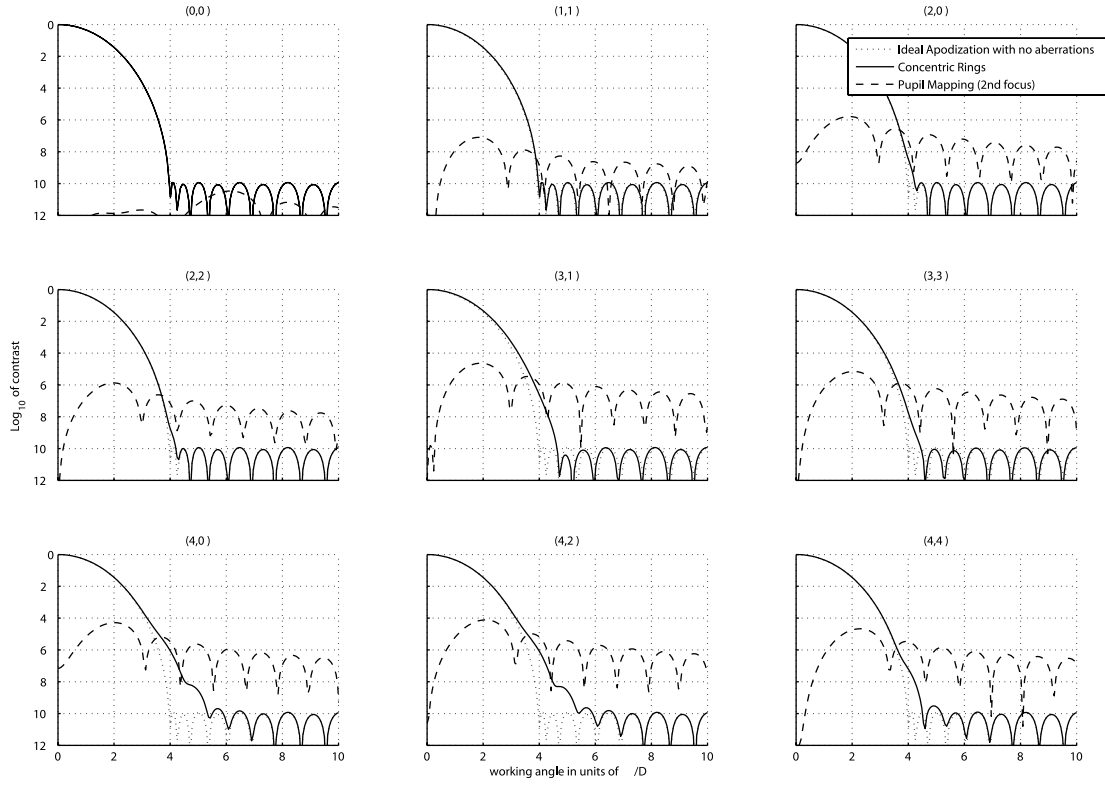
FIG. 11.—Radial profiles associated with Figs. 9 and 10 overlaid one on the other. The dashed plots are for apodized pupil mapping, whereas the solid plots are for the concentric-ring mask. [*See the electronic edition of the Journal for a color version of this figure.*]
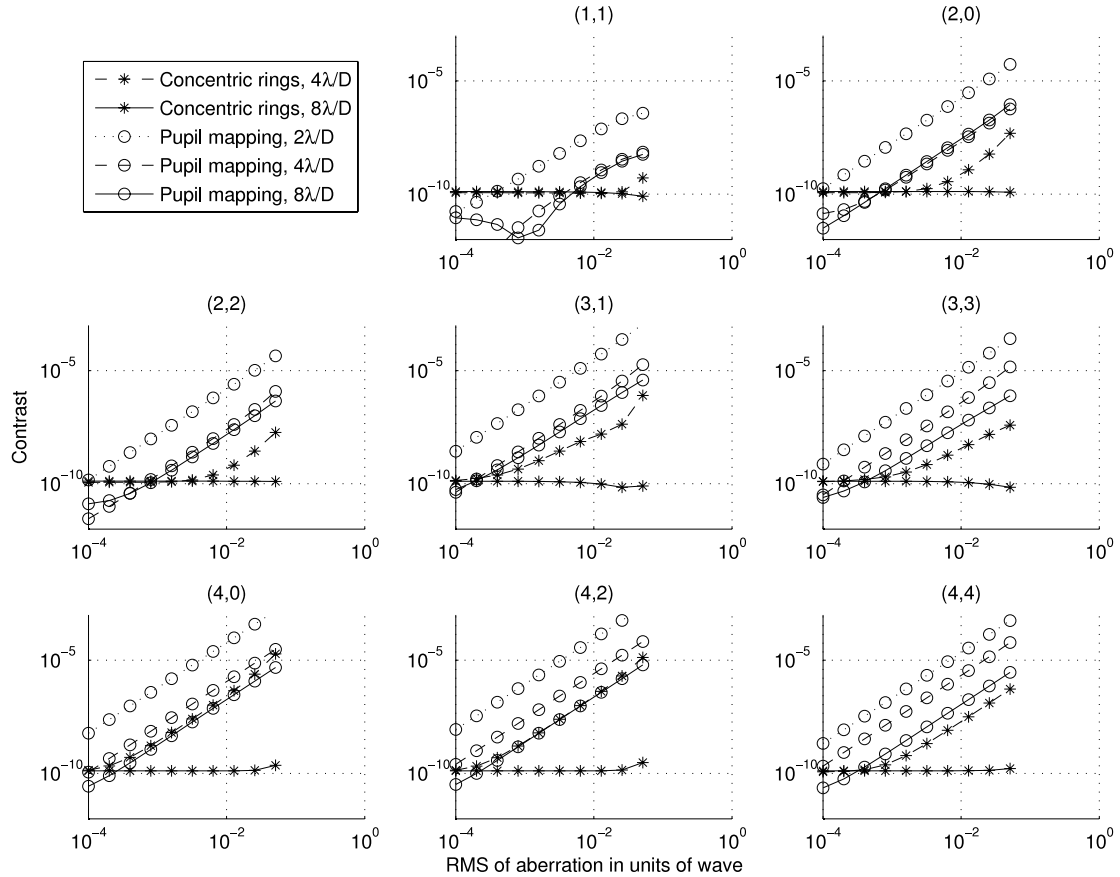

FIG. 12.—Contrast degradation measured at three angles, $2\lambda/D$, $4\lambda/D$, and $8\lambda/D$ as a function of severity of the Zernike wave front error measured in waves. [*See the electronic edition of the Journal for a color version of this figure.*]

REFERENCES

Born, M., & Wolf, E. 1999, Principles of Optics (7th ed.; New York: Cambridge Univ. Press)
Green, J. J., Shaklan, S. B., Vanderbei, R. J., & Kasdin, N. J. 2004, Proc. SPIE, 5487, 1358
Guyon, O. 2003, A&A, 404, 379
Guyon, O., Pluzhnik, E. A., Galicher, R., Martinache, R., Ridgway, S. T., & Woodruff, R. A. 2005, ApJ, 622, 744
Jacquinot, P., & Roizen-Dossier, B. 1964, Prog. Optics, 3, 29
Kasdin, N. J., Vanderbei, R. J., Spergel, D. N., & Littman, M. G. 2003, ApJ, 582, 1147
Kuchner, M. J., Crepp, J., & Ge, J. 2005, ApJ, 628, 466
Nisenson, P., & Papaliolios, C. 2001, ApJ, 548, L201

Pluzhnik, E. A., Guyon, O., Ridgway, S. T., Martinache, F., Woodruff, R. A., Blain, C., & Galicher, R. 2006, ApJ, 644, 1246
Shaklan, S. B., & Green, J. J. 2005, ApJ, 628, 474
Shao, M., Levine, B. M., Serabyn E., Wallace, J. K., & Liu, D. T. 2004, Proc. SPIE, 5487, 1296
Slepian, D. 1965, J. Opt. Soc. Am., 55, 1110
Soummer, R., Aime, C., & Falloon, P. E. 2003, A&A, 397, 1161
Traub, W. A., & Vanderbei, R. J. 2003, ApJ, 599, 695
Vanderbei, R. J. 2006, ApJ, 636, 528
Vanderbei, R. J., Kasdin, N. J., & Spergel, D. N. 2004, ApJ, 615, 555
Vanderbei, R. J., Spergel, D. N., & Kasdin, N. J. 2003, ApJ, 599, 686
Vanderbei, R. J., & Traub, W. A. 2005, ApJ, 626, 1079